Journal of Materials Chemistry B

Accepted Manuscript

ROYAL SOCIETY OF CHEMISTRY

www.rsc.org/materialsB

Graphical Abstract

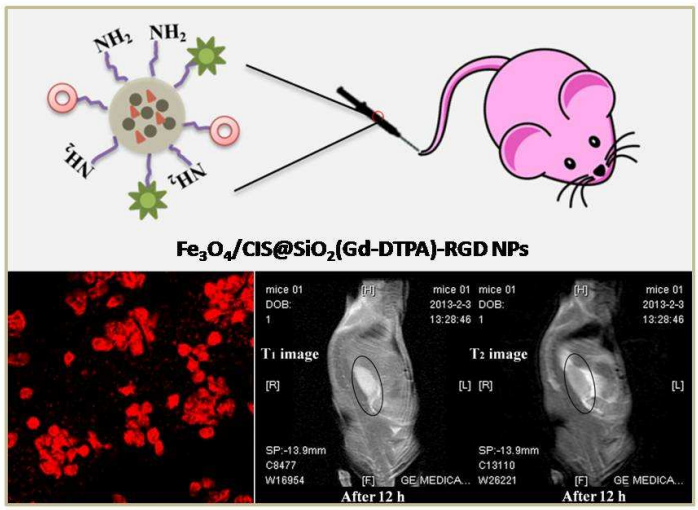

A facile fabrication of Gd-labeled surperparamagnetic Fe_3O_4 nanoparticles (NPs) and florescence $CuInS_2$ (CIS) quantum dots conjugated with argininеglycine-aspartic acid (RGD) peptides for tri-mode targeted T_1-, T_2-weighted magnetic resonance (MR) and fluorescent imaging of pancreatic cancer.

Cite this: DOI: 10.1039/c0xx00000x

www.rsc.org/xxxxxx

ARTICLE TYPE

Multifunctional Gadolinium-Labeled Silica-Coated Fe_3O_4 and $CuInS_2$ Nanoparticles as a Platform for In Vivo Tri-Modality Magnetic Resonance and Fluorescence Imaging

Jianhua Shen,[a] Yunfeng Li,[a,b] Yihua Zhu,*[a] Xiaoling Yang,[a] Xiuzhong Yao,[c] Jun Li,[c] Guangjian Huang[d] and Chunzhong Li*[a]

Received (in XXX, XXX) XthXXXXXXXXX 20XX, Accepted Xth XXXXXXXXX 20XX
DOI: 10.1039/b000000x

A facile fabrication of Gd-labeled surperparamagnetic Fe_3O_4 nanoparticles (NPs) and florescence $CuInS_2$ (CIS) quantum dots conjugated with argininеglycine-aspartic acid (RGD) peptides for tri-mode targeted T_1-, T_2-weighted magnetic resonance (MR) and fluorescent imaging of pancreatic cancer has been demonstrated. The formed core-shell nanocomposites are water-dispersible, stable, and biocompatible as confirmed by MTT assay on BXPC-3 cells. Relaxivity measurements show a T_1 relaxivity (r_1) of 1.56 mM^{-1} s^{-1} and T_2 relaxivity (r_2) of 23.22 mM^{-1} s^{-1}, which enable T_1- and T_2-weight MR imaging of cancer cells in vitro and in vivo. The MR imaging data clearly indicate that the multifunctional NPs can specifically target to cancer cells with $\alpha_v\beta_3$ integrin over-expression on the cell surface through receptor-mediated delivery pathway. The T_1-weight positive and T_2-weighted negative enhancement in the MR imaging significantly improve the diagnosis accuracy, and fluorescent imaging of tumor tissue can assist in the clinical surgery. These findings suggest that these multifunctional NPs could be used as a platform for bimodal imaging (both MR and fluorescence) in various biological systems.

1. Introduction

Pancreatic adenocarcinoma is the seventh most common cause of deaths due to cancer. More than 80% of patients, diagnosed with this pancreatic cancer, have locally advanced or metastatic disease and are unsuitable for curative surgical resection. As a result of dismal prognosis in pancreatic cancer, median survival for locally advanced disease is just 6-10 month, and this value falls to 3-6 months for patients with metastatic disease. Overall 5 year survival is less than 4%.[1] In spite of significant improvements in operative techniques and postoperative mortality rates, the overall survival for these patients has not changed significantly.[2] So methods for the accurate detection of pancreatic cancer at early stage are of importance and are an active area of current research, which improvement in surgical morbidity and mortality and the introduction of promising adjuvant and neoadjuvant therapies.[3] Although imaging modalities, such as ultrasound (US), computed tomography (CT), magnetic resonance imaging (MRI), have evolved markedly in recent years, the knowledge of pancreatic cancer known to radiologists is only based on its morphological changes through imaging.[4]

Among the various imaging techniques, MRI has been recognized to be one of the most powerful medical diagnosis tools because MRI can provide images with excellent anatomical details based on the soft tissue contrast and functional information in a noninvasive and real-time monitoring manner.[5,6] The current MRI contrast agents are generally in the form of T_1 positive agents of paramagnetic species and T_2 negative agents of superparamagnetic particles. Paramagnetic compounds with large number of unpaired electrons including Gd^{3+}, Mn^{2+} are desirable for T_1 contrast because T_1 contrast effect is induced by the interactions between protons of water molecules and electron spins of the contrast agents.[7,8] Gadolinium complexes, having 7 unpaired electrons in its Gd^{3+} core, are widely used as T_1 contrast agent.[9] The complexes generally have short circulating time due to the rapid excretion through urine, which hampers the high-resolution imaging that requires long scan time.[10] Therefore, nanoparticles-based agents that can be internalized into living cells could be used as a powerful platform to significantly increase the imaging time.[11] On the other hand, T_2 contrast agents have also been received a great attention over the last 20 years. Superparamagnetic iron oxide NPs with superior magnetic properties have emerged as a prevailing agent so far.[12] However, these magnetic NP-based agents give a signal-decreasing effect, and the high susceptibility limits their extensive clinical applications. In addition, considering the different penetration depths and spatial/time resolutions of multiple imaging devices, a

new strategy towards the development of NP-based dual mode contrast agent, where two different modes of imaging (T_1- and T_2-weight MR imaging) are utilized simultaneously, is necessary and amenable for significant improvement of the diagnosis accuracy. Recently, Lee and coworkers reported an approach to fabricate Fe_3O_4/MnO hybrid nanocrystals as dual-contrast agents for T_1- and T_2- weighted MR imaging.[13] Yang and coworkers demonstrated Gd-labeled superparamagnetic Fe_3O_4 NPs for dual mode targeted T_1- and T_2-weighted MR imaging of cancer cells in vitro and vivo.[14] These formed multifunctional NPs are water-dispersible, stable, and with modification of argininegly cine-aspartic acid (RGD) onto their surfaces. Despite the attractive properties, sensitivity of the corresponding MRI is relatively poor for low levers of molecular targets and suffers from a lack of cell specificity compared to other imaging modalities. Therefore, the developing of novel NPs-based multimodal imaging probes to meet the clinical requirements still remains a great challenge for meeting accurate imaging and diagnosis for the clinical requirements.[15,16]

Comparatively, fluorescence imaging has the excellent sensitivity at subcellular levels and for quantifying molecular events, but its limited capability in examining deep tissue restricts collection of information in vivo. Therefore, an integrated nanoprobe, useful for both MR and fluorescence imaging, would lead to novel tools for imaging technologies due to the highly complementary capabilities. Yang et al. prepared silica-coated manganese oxide NPs conjugation of Rhodamine B isothiocyanate and folate onto their surface for dual mode targeted MR and fluorescence imaging.[17] Further, more research focused on semiconductor quantum dots owing to their excellent photostability over molecular fluorophores.[18-20] For instance, MRI/ fluorescence NPs have been designed that involve attachment of Gd^{3+} chelates to CdSeTe/CdS,[21] CdSe,[22–24] CdTe/ZnS quantum dots.[25] However, their widespread biological use is severely limited by the presence of cadmium.[26] $CuInS_2$ (CIS) quantum dots are emerging as one such promising candidate. They do not contain toxic elements and, being direct band-gap semiconductors, the optical properties can be tuned by composition and size.

For biological applications, the NPs-based imaging platforms should be water-dispersible and biocompatible, and have reactive surface groups for further bioconjugation. The silica shell on NPs can not only protect the core NPs from the external environment, but also are highly biocompatible and their surface can be easily modified with amines, thiols, and carboxyl groups, which enables covalent modification of the particle surfaces with biological molecules.[27, 28] Another important aspect in the use of NP-based platforms for biomedical imaging is the ability to target pancreatic cancer tissues. Among the neoplastic markers that are currently under investigation, $\alpha_v\beta_3$ integrin is of particular interest.[29, 30] $\alpha_v\beta_3$ integrin can bind with argininegly cine-aspartic acid (RGD) in an extracellular matrix. A number of NPs-RGD conjugates have been developed for a variety of imaging due to their high density in activated tumor vessels and at low density in reststage endothelial cells in pancreatic cancer tissues.[31, 32]

Herein, we develop a novel multifunctional Gd-labeled superparamagnetic Fe_3O_4 NPs and CIS quantum dots for targeted tri-mode T_1- T_2-weighted MR and fluorescence imaging of pancreatic neoplasm. Firstly, we utilized the thermal decomposition approach to synthesize Fe_3O_4 NPs and CIS quantum dots. Then these NPs were coated by the silica shell. The silica-coated NPs were aminated through silanization, which enabled further conjugation of Gd^{3+}-DTPA (diethylenetriaminepentaacetic acid) complex and RGD peptide onto their surface (Scheme 1). The formed multifunctional Fe_3O_4/CIS@SiO_2(Gd-DTPA)-RGD NPs were characterized using X-ray diffraction (XRD), transmission electron microscopy (TEM), fluorescence spectroscopy, and relaxivity measurements. The cellular imaging of Fe_3O_4/CIS@SiO_2(Gd-DTPA)-RGD NPs was also successfully demonstrated by using human pancreatic cancer cell lines BXPC-3 cells, and the targeting specificity were evaluated by T_1- and T_2-weighted MR imaging in vitro and in vivo.

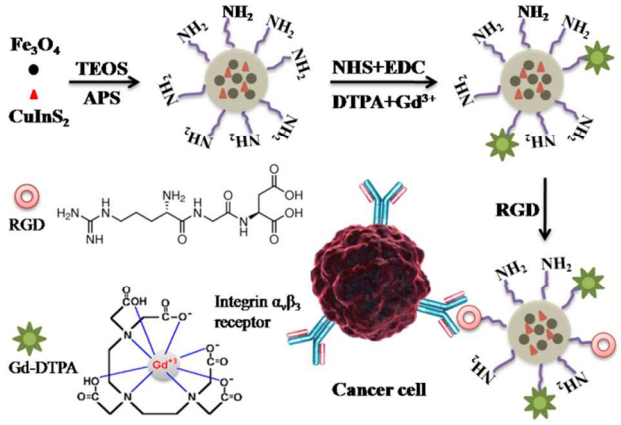

Scheme 1 Schematic illustration the formation of Fe_3O_4/CIS@SiO_2(Gd-DTPA)-RGD NPs.

2. Experimental Section

2.1 Synthesis of Fe_3O_4 NPs. Iron-oleate complex was synthesized according to the previously reported procedure.[33] For the synthesis of 8 nm-sized iron oxide NPs, iron-oleate (4 mmol), 1-octadecene (20 g, Aldrich, 90 %) and oleic acid (4 mmol, Aldrich, 90 %) were put into a three-neck flask at room temperature. The reaction mixture was degassed under vacuum at 120 °C for 30 min to remove water sufficiently. Subsequently, the solution was heated up to 320 °C with a constant heating rate of 2.5 °C min^{-1} under a nitrogen atmosphere. A severe reaction occurred and the initial transparent solution became turbid and brownish black, and then kept the mixtures at this temperature for 10 min before cooling down to room temperature. The iron oxide NPs were precipitated upon adding 20 mL ethanol and washed three times with ethanol and hexane. The as-prepared iron oxide NPs were finally dispersed in chloroform.

2.2 Synthesis of $CuInS_2$ quantum dots. Cu(I) iodide (0.4 mmol, CuI, 99.998%), In(III) acetate (0.4 mmol, $In(OAc)_3$, 99.99%) 1-dodecanethiol (0.85 g) and 1-octadecene (6.31 g) were put into a 50 mL three-neck under a nitrogen atmosphere.[34,35] The mixture was heated to 80 °C under a vacuum and magnetic stirring for 1 h, backfilled with N_2, and heated to the reaction temperature of

230 °C with a constant heating rate of 4 °C min^{-1}. The color of the reaction solution progressively changed from colorless to green, yellow, red, and finally dark brown. The growth of $CuInS_2$ quantum dots was allowed for 20 min. As-reacted $CuInS_2$ quantum dots were precipitated with an excess of ethanol, purified repeatedly with a solvent combination of chloroform-ethanol by a centrifugation, and finally also dispersed in chloroform.

2.3 Formation and functionalization of Fe_3O_4/CIS@SiO_2 core-shell nanocomposites. The silica coating process was adopted from the published papers with some modifications.[36,37] 1 mL solution of chloroform containing 10 mg of $CuInS_2$ quantum dots and 1 mL solution of chloroform containing 15 mg of Fe_3O_4 was added to 10 mL 0.25 M cetyltrimethylammonium bromide (CTAB) solution. After vigorous vortex and sonification for 40 min, the opaque solution became semitransparent gel. The gel was then heated to 70 °C to evaporate the chloroform, leaving a transparent deep reddish-brown solution. The formed solution was added to a mixture of 45 mL of water and 0.3 mL of 2 M NaOH solution. The mixture was then heated 70 °C. Subsequently, TEOS (0.75 mL) and ethylacetate (5 mL) were dropped into the reaction solution. The reaction was kept on stirring for 3 h, and then APS (0.15 mL) was added. The mixture was further stirred for 30 min and allowed to slowly cool down to room temperature, and finally acetone was added to collect the particles. The collected aminated Fe_3O_4/CIS@SiO_2-NH_2 NPs were dispersed in ethanol or water and purified by repeating the centrifugation and redispersion process. The product was stored in ethanol solution.

2.4 Loading Gd^{3+} ions to DTPA-functionalied nanocomposites. For the further loading of Gd^{3+}, the diethylenetriaminepentaacetic acid (DTPA) moieties were used to modify the surface of the obtained NPs to form the DTPA-Gd^{3+} complex. The Fe_3O_4/CIS@SiO_2-NH_2 NPs (30 mg) were dispersed into dry DMF (16 mL). Then, triethylamine (0.36 mL) and diethylenetriaminepentaacetic acid dianhydride (DTPAda) (72 mg) was added to the NPs suspension. The mixture was heated to 80 °C for 30 min, and cooled down to room temperature while stirring overnight. The NPs were purified by repeating the centrifugation/redispersion/washing steps: 2 times with 1 % triethylamine in DMF, 2 times with water, and 2 times with acetone, followed by drying in vacuum before use. By varying the concentration of DTPAda, Fe_3O_4/CIS@SiO_2-NH_2 NPs were obtained. The DTPA-functionalized NPs were stored at 4 °C before use.

The prepared Fe_3O_4/CIS@SiO_2(DTPA)-NH_2 NPs (30 mg) were dispersed in Tris–HCl buffer solution (pH = 7.4, 15 mL, 0.05 M). Then, a $Gd(NO_3)_3{\cdot}6H_2O$ aqueous solution (1.5 mL, 10 mM), were added dropwise into the NPs suspension while stirring. Gd^{3+} ions were anchored onto the surface by linking Gd^{3+} via a strong chelation bond with carboxyl groups of DTPA. After 12 h, these NPs were centrifuged and redispersed in water for at least three times. The obtained Gd^{3+}-loaded Fe_3O_4/CIS@SiO_2(DTPA)-NH_2 NPs were finally dispersed in water to form a pale white transparent solution.

2.5 Synthesis of RGD-labeled Fe_3O_4/CIS@SiO_2(Gd-DTPA) NPs. To modify the remaining surface amine groups of the Fe_3O_4/CIS@SiO_2(Gd-DTPA)-NH_2 NPs, 6-maleimidohexanoic acid N-hydroxysuccinimide ester (31 mg, 1 mmol) was added to an HEPES (4-(2-hydroxyethyl)-1-piperazineethanesulfonic acid) buffer solution (0.1 mol L^{-1}, 5 mL, pH = 8.0) containing the Fe_3O_4/CIS@SiO_2(Gd-DTPA)-NH_2 NPs while stirring at room temperature. After 8 h, the particles were centrifuged and washed twice with water. The precipitate was then redispersed into HEPES buffer (5 mL), followed by adding an HEPES buffer solution (0.1 mol L^{-1}, 5 mL, pH = 7.3) containing thiolated cyclo(Arg-Gly-Asp-Phe-Lys(mpa)) (c(RGDFK)) peptide (69 mg, 1.0 mmol), while gently stirring at room temperature for 12 h. The mixture was centrifuged and washed twice with water to purify the RGD-labeled Fe_3O_4/CIS@SiO_2(Gd-DTPA) NPs. The purified particles were resuspended in HEPES buffer (0.1 mol L^{-1}, 5 mL, pH = 7.3) and stored at 4 °C before use.

2.6 Characterization. The morphology and microstructure of the samples were investigated by High-transmission electron microscopy (TEM: JEM-2100, operated at 200 kV) and Scanning electron microscopy (FE-SEM: S-4800). PL spectra were obtain on a Cary Eclipse (Varian) Fluorescence spectrophotometer. XRD was obtained by wide-angle X-ray scattering using a Siemens D5005 X-ray powder diffractometer equipped with graphite-monochromatized Cu kα radiation (λ = 1.54178 Å). XRD samples were prepared by depositing nanoparticles power on a piece of Si(100) wafer. ICP-AES (optima 7300DV, Perkin-Elmer) was used to measure the concentrations of Gd and Fe elements in the samples. MRI was obtained by NMR relaxivity. MRI imaging experiments were performed at room temperature on a biospec 3T system equipped with the standard gradient set.

2.7 Cytotoxicity testing and in vitro microscopy imaging. A cell counting Kit-8 assay kit (Beyotime, China) was employed to evaluate the toxicity of the samples. Briefly, the cells were seeded into a 96-well plate (Corning, USA) and grown to a density of 10^4 cells per well. Then serial dilutions of the samples were added and co-incubated with the cells for 24 h. Subsequently, CCK-8 solution (20 mL per well) was added and the plate was further incubated for 30 min. The absorbance of each well at 450 nm was finally measured with a microplate reader (Infinite M200, Tecan).

Human pancreatic cancer cell lines BXPC-3 cells were placed in a 96-well plate, and grown at 37 °C and 5 % CO_2 in air. After seeding 24 h, 100 μL of nanoparticles with the concentration of 10 μg mL^{-1} were added to each well. After incubation for 3 h, the cells were observed using an Olympus Fluoview 300 confocal laser scanning system with 488 nm argon laser excitation.

2.8 Relaxivity measurements. To optimize the relaxation characteristics of the Fe_3O_4/CIS@SiO_2(Gd-DTPA)-RGD NPs as dual MR contrast agents at various iron concentrations. All samples were diluted in normal saline (0.9 % w/v NaCl, pH = 7.4) solution. All MR relaxivity measurements were performed with a 3.0 T systems. T_1-weighted MR images were acquired using a conventional spin-echo sequence under the following parameters: TR/TE = 500/12 ms, 320 × 320 matrices, 130 × 130 mm field of view, 140 Hz/Px of bandwidth, a slice thickness of 3

mm. T_2-weighted MR images using a fast spin-echo sequence was used to reduce acquisition time under the following parameters: TR/TE = 3000/11 ms, 256 × 256 matrices, 180 × 180 mm field of view and 220 Hz/Px of bandwidth, a slice thickness of 3 mm. The specific relaxivity values of r_1 and r_2 were calculated through the curve fitting of $1/T_1$ and $1/T_2$ (s^{-1}) vs the Fe concentration (mM).

2.9 In vivo MR imaging. To verify the dual-contrast ability of Fe_3O_4/CIS@SiO_2(Gd-DTPA)-RGD NPs for targeted imaging of the pancreatic adenocarcinoma model in vivo. Animal procedures were in agreement with the guidelines of the Institutional Animal Care and Use Committee. Animal studies were performed using adult nude mouse (20-30 g, from Zhongshan Hospital of Fudan University). Subcutaneous xenografts were produced in animals by subcutaneous injection of 1×10^6 BxPC-3 cells in 100 μL of serum-free cell culture medium in subaxillary. Animals were studied when the sizes of the subcutaneous tumor xenografts were approximate 1-1.2 cm in diameter after ten days. In vivo MR imaging experiments were performed using a 3.0 T systems. A 200 mL of the Fe_3O_4/CIS@SiO_2(Gd-DTPA)-RGD NP suspension (2 mg/mL) was injected into nude mice through tail vein injection. T_1-weighted MR images were acquired using a conventional spin-echo sequence with the following parameters: TR/TE = 500/11 ms, 320× 320 matrices, 60× 60 mm field of view, 140 Hz/Px of bandwidth, a slice thickness of 2 mm. For T_2-weighted MR imaging, a fast spin-echo sequencewas used to reduce acquisition time with the same parameters of T_1-weighted MRI, except for TR/TE = 4000/89 ms and 220 Hz/Px of bandwidth. Each in vivo scan was completed within half an hour.

3. Results and Discussion

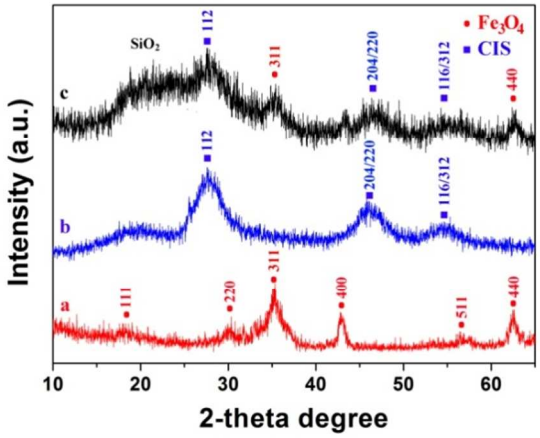

Fig. 1 X-ray diffraction pattern of (a) Fe_3O_4 NPs, (b) CIS quantum dots, and (c) Fe_3O_4/CIS@SiO_2-NH_2 NPs.

3.1 Synthesis and characterization of Fe_3O_4/CIS@SiO_2(Gd-DTPA)-RGD NPs. The iron oxide NPs were prepared according to the method reported by Park et al.[33] And $CuInS_2$ quantum dots were prepared following the previous protocols by using 1-dodecanethiol (DDT), containing long hydrocarbon tails as a hydrophobic protective agent and ODE as solvent.[38] The crystallography of the products was verified by powder X-ray diffraction (XRD) (Fig. 1). It is clear that the positions and relative intensity of all diffraction peaks match well with (111), (220), (311), (400), (511), (440) planes of standard Fe_3O_4 powder diffraction data (JCPDS, 85–1436), respectively. And as shown in Fig. 1b, three distinct reflection peaks with 2θ values of 28.0, 46.5, and 54.9° could be indexed well to the (112), (204)/(220), and (116)/(312) planes of a known tetragonal chalcopyrite structure of the $CuInS_2$ phase (JCPDS card No. 85-1575).[39] The broadening of the diffraction peaks distinctly indicates the nanocrystalline nature. The Fe_3O_4 NPs and CIS quantum dots were modified with silica shells to achieve water solubility. By treating the Fe_3O_4 NPs and CIS quantum dots with both tetraethyl orthosilicate (TEOS) and (3-aminopropyl) triethoxysilane (APS), Fe_3O_4/CIS@SiO_2 particles with surface amine groups were formed. The XRD pattern of the aminated particles (Fig. 1c) confirms the existence of Fe_3O_4, CIS and amorphous silica. A broad peak from ca. 22 to 28° indicates the successful encapsulation of silica onto the Fe_3O_4 and CIS surface.

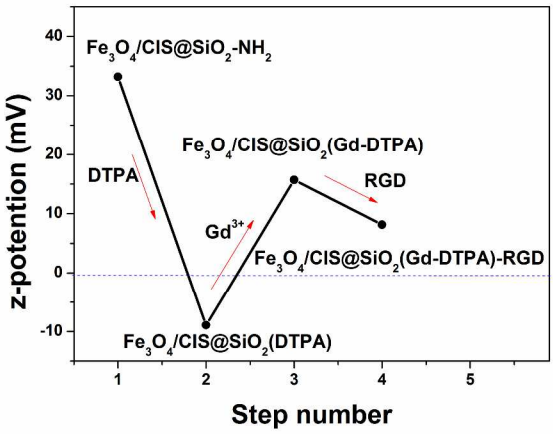

Fig. 2 The zeta-potential *vs.* each functionalization step number of Fe_3O_4/CIS@SiO_2(Gd-DTPA)-RGD NPs at pH=7.

To investigate the conjugation of Gd complex and RGD peptide onto the surface of Fe_3O_4/CIS@SiO_2-NH_2 NPs, the NPs after each functionalization step were studied by zeta potential measurements. As shown in Fig. 2, the surface potential of the particles varies from +33.2 mV (Fe_3O_4/CIS@SiO_2-NH_2) to -8.9 mV (Fe_3O_4/CIS@SiO_2(DTPA)) and +15.7 mV (Fe_3O_4/CIS@SiO_2(Gd-DTPA)), respectively. And after the formation of Fe_3O_4/CIS@SiO_2(Gd-DTPA)-RGD NPs, the surface potential further decreases from +15.7 mV to +8.16 mV. The aminated Fe_3O_4/CIS@SiO_2-NH_2 NPs with a positive surface potential (+33.2 mV) is reversed to a negative surface potential (-8.9 mV) after grafting with DTPA, which can be explained by the surface coverage of the particles with negatively charged DTPA ligand. Further the complexation with Gd^{3+} gave rise to a slightly positive surface potential of +15.7 mV, presumably due to the coordination of Gd^{3+} with the carboxylate groups of DTPA ligand, resulting in the neutralization of the negative surface charge.[40] Finally, the z-potential of the obtained Fe_3O_4/CIS@SiO_2(Gd-DTPA)-RGD NPs changed to +8.16 mV, which was suggested that the remaining surface amine groups on the Fe_3O_4/CIS@SiO_2(Gd-DTPA)-NH_2 NPs have been modified with RGD moieties.[14]

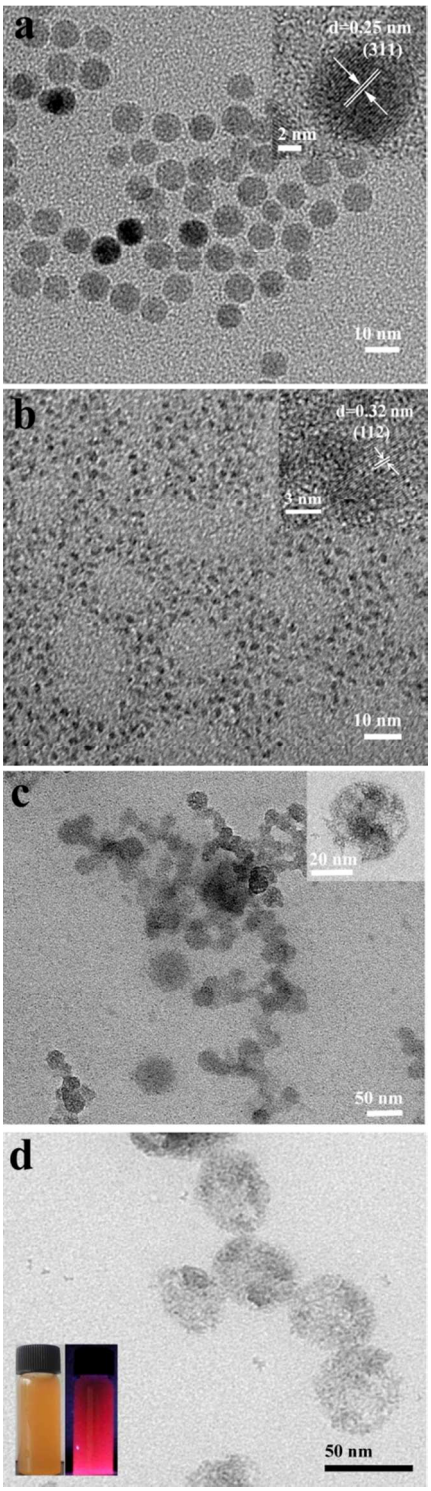

Fig. 3 (a) TEM micrograph of Fe_3O_4 NPs. Inset: high-resolution TEM image of Fe_3O_4 NP; (b) TEM micrograph of CIS quantum dots. Inset: high-resolution TEM image of CIS quantum dot; (c) TEM micrograph of Fe_3O_4/CIS@SiO_2-NH_2 NPs. Inset: high-resolution TEM image of Fe_3O_4/CIS@SiO_2-NH_2 NP; (d) TEM micrograph of Fe_3O_4/CIS@SiO_2(Gd-DTPA)-RGD NPs. Inset: the visual photograph of Fe_3O_4/CIS@SiO_2(Gd-DTPA)-RGD NPs in normal saline solution (left), and the red emission of Fe_3O_4/CIS@SiO_2(Gd-DTPA)-RGD NPs in normal saline solution under the 365 nm portable UV lamp excitation, these solutions were kept at room temperature for 3 months.

The Fe_3O_4 NPs are monodispersed and have a spherical shape with a diameter of ca. 7 nm (Fig. 3a). High-resolution TEM image (Fig. 3a inset) of the particles reveals the highly crystalline nature of Fe_3O_4 NPs. The lattice spacing between two adjacent planes is 0.25 nm, which corresponds very well to the *d* spacing for the (311) lattice plane. It is consistent with the spinel-structured Fe_3O_4 and matches the XRD data well. Fig. 3b presents a TEM image of representative $CuInS_2$ quantum dots with a diameter in the range of 2.0-3.0 nm. Such a size distribution is usually inherent in the non injection-based synthetic route and can be partially attributed to a continual release of the S ion from the DDT molecule throughout the reaction. We also investigated the high resolution TEM image of typical $CuInS_2$ with a lattice spacing of 0.32 nm, which corresponds to the (112) face of the $CuInS_2$ orthorhombic structure (Fig. 3b inset). The reverse microemulsion method was used to prepare Fe_3O_4/CIS@SiO_2-NH_2 NPs as described in the Experimental section. Fig. 3c displays the TEM image of the aminated Fe_3O_4/CIS@SiO_2-NH_2 NPs. Calculated from the observation of the TEM image, the average diameter of the Fe_3O_4/CIS@SiO_2-NH_2 NPs was around 45 nm. Owing to the toxicity to the cultivated cells, the CTAB was removed by repeatedly washing the NPs with ethanol and water to diminish their cell toxicity for further biological applications. As shown in Fig 3c inset, the particles reveals the structure of Fe_3O_4/CIS@SiO_2-NH_2 NPs, the diameter is around 40 nm, indicating that silica was coated onto the surface of both Fe_3O_4 and CIS NPs. For conjugation of Gd^{3+} complex onto the surface of Fe_3O_4/CIS@SiO_2-NH_2 NPs, DTPA was reacted with the primary amine group of Fe_3O_4/CIS@SiO_2-NH_2 NPs through the formation to amide bonds.[41] To complex Gd^{3+} via a strong chelation bond with carboxyl groups of DTPA, the DTPA-conjugated Gd^{3+} were mixed with an excess amount of $Gd(NO_3)_3{\cdot}6H_2O$ and free Gd^{3+} ions were removed by dialysis. In render the nanocomposites with targeting capability for their biological application, RGD was conjugated with the Fe_3O_4/CIS@SiO_2(Gd-DTPA) nanocomposites. Fig. 3d shows the Fe_3O_4/CIS@SiO_2(Gd-DTPA)-RGD NPs attained the similar size distribution to the Fe_3O_4/CIS@SiO_2-NH_2 NPs (Fig. 3c). In addition, due to multiple surface modification and processing, the Fe_3O_4/CIS@SiO_2(Gd-DTPA)-RGD nanocomposites display the better dispersion. The Gd/Fe/Cu molar ratio was estimated by inductively coupled plasma atomic emission spectroscopy (ICP-AES). It was revealed that the formed 1 mg/mL Fe_3O_4/CIS@SiO_2(Gd-DTPA)-RGD NPs had 0.113 mM Gd, 1.20 mM Fe and 0.383 mM Cu. The formed Fe_3O_4/CIS@SiO_2(Gd-DTPA)-RGD NPs are water-dispersible and colloidally stable in normal saline solution for at least 3 months at room temperature (Fig. 3d inset), and the red emission of Fe_3O_4/CIS@SiO_2(Gd-DTPA)-RGD NPs was shown under the 365 nm portable UV lamp excitation, which is essential for biological applications.

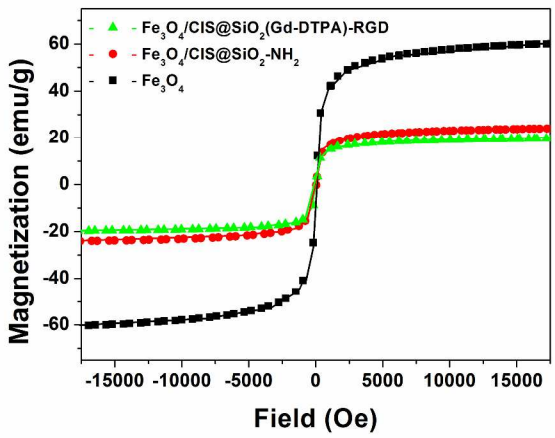

Fig. 4 Room temperature hysteresis loop of Fe_3O_4 NPs, Fe_3O_4/CIS@SiO_2-NH_2 NPs and Fe_3O_4/CIS@SiO_2(Gd-DTPA)-RGD NPs.

3.2 The properties of Fe_3O_4/CIS@SiO_2(Gd-DTPA)-RGD NPs.

The magnetic property of NPs was evaluated by field-dependent magnetization measurements at room-temperature (Fig. 4). The magnetization saturation values were measured to be 60.5, 25.5, and 19.9 emu/g for Fe_3O_4, Fe_3O_4/CIS@SiO_2-NH_2, and Fe_3O_4/CIS@SiO_2(Gd-DTPA)-RGD, respectively. The lack of hysteresis loops indicates the superparamagnetic nature of the NPs. The saturated magnetization of Fe_3O_4/CIS@SiO_2-NH_2 was much smaller than the value of the Fe_3O_4 NPs. The reduced saturation magnetization of the NPs is generally believed to be due to the CIS quantum dots coupling and silica coating, resulting in decreased magnetic anisotropy, in agreement with literature.[42] After Gd-DTPA and RGD conjugation onto the surface of the NPs, the saturated magnetization of Fe_3O_4/CIS@SiO_2(Gd-DTPA)-RGD decreased to 19.9 emu/g, which is probably attributed to the decrease of iron oxide content in the particles.[43]

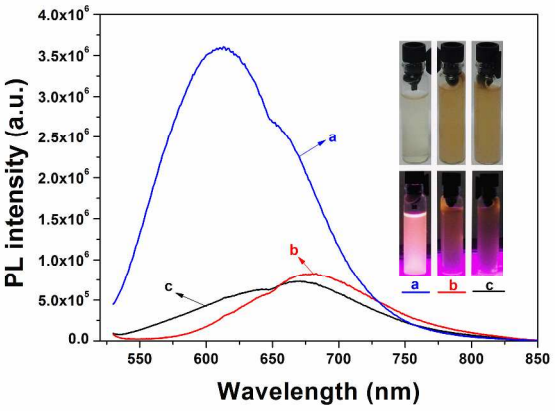

Fig. 5 Room temperature luminescence spectra of CIS quantum dots (Curve a), Fe_3O_4/CIS@SiO_2-NH_2 NPs (Curve b) and Fe_3O_4/CIS@SiO_2(Gd-DTPA)-RGD NPs (Curve c) in water under the 470 nm excitation. Insets: visual photographs of CIS quantum dots (a), Fe_3O_4/CIS@SiO_2-NH_2 NPs (b) and Fe_3O_4/CIS@SiO_2(Gd-DTPA)-RGD NPs (c) in water under the 365 nm portable UV lamp excitation.

Optical properties of the obtained NPs, shown in Fig. 5, indicate that shell formation was successful. The red fluorescence (620 nm) was observed because of emitting red luminescence of CIS quantum dots under UV irradiation (365 nm), and the quantum yield was measured to be 8.2 %. It is worth noticing that the PL emission spectra of the Fe_3O_4/CIS@SiO_2-NH_2 NPs demonstrated the red shift unexceptionally (Fig. 5b). The PL emission red shifts of silica coated CdSe and CdTe synthesized by the reverse microemulsion method were reported by other researchers previously. Although the mechanism remains unclear, this change in PL spectra is usually attributed to the ligand replacement and change in surface charge.[44] It is well known that surfactants play an important role in surface passivation by forming bonds with exposed atoms on the surface and protecting surface defects. Therefore, the change in the surface state greatly affects the photophysical properties of quantum dots. Besides, several investigations have proven that charges, especially negative charges, in the vicinity of quantum dots can generate an electric field which is sufficient to influence the radiative recombination rate of electron-hole pairs.[44] Subsequently, the emission spectra of quantum dots can be quenched and red-shifted. In addition, no obvious luminescence change was observed between Fe_3O_4/CIS@SiO_2-NH_2 NPs and Fe_3O_4/CIS@SiO_2(Gd-DTPA)-RGD NPs (Fig. 5c).

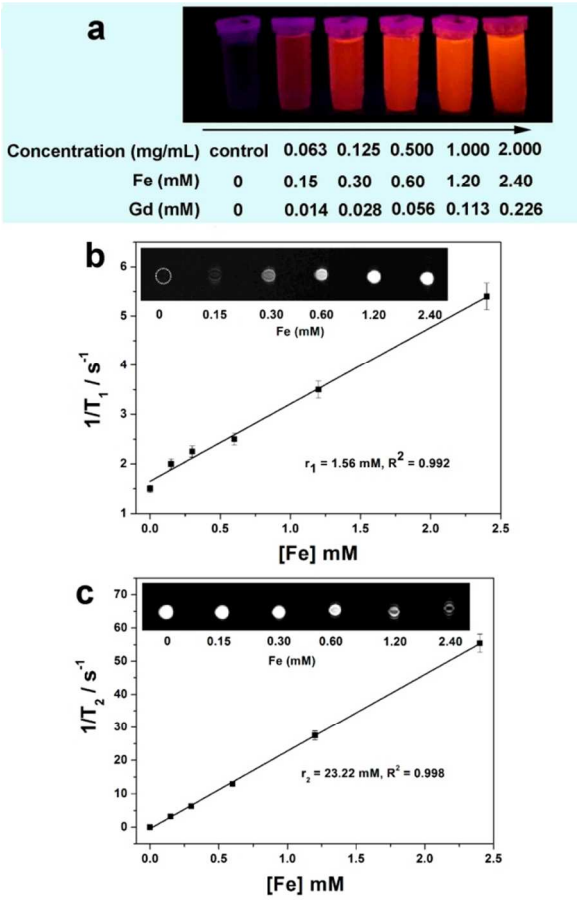

Fig. 6 (a) the corresponding optical detection. By eye, nanoparticles at 0.063, 0.125, 0.500, 1.000 and 2.000 mg mL^{-1} (left to right), illuminated by a handheld UV lamp, show no decrease in emission intensity with dilution. (b) T_1 relaxivity plot of aqueous suspension of Fe_3O_4/CIS@SiO_2(Gd-DTPA)-RGD NPs, inset: T_1 weighted MR images of the nanoparticles in water at different concentration of NPs. (c) T_2 relaxivity plot of aqueous suspension of Fe_3O_4/CIS@SiO_2(Gd-DTPA)-RGD NPs, inset: signal intensity analysis for T_2-weighted MR images.

The formed Fe_3O_4/CIS@SiO_2(Gd-DTPA)-RGD NPs were well dispersed in water, and the optical photography of the nanoparticles at different concentrations are shown in Fig. 6a. The samples of the same concentrations of NPs employed for the MR studies were photographed using only a handheld UV lamp as excitation. It is clear that there is no detectable difference in intensity between concentrations, suggesting that even the lowest concentration saturated the detector by eye. The MRI mechanisms are based on excitation and relaxation of hydrogen nuclei that are abundant in water and lipids of tissue. The intrinsic longitudinal (T_1) and transverse (T_2) relaxation times of different parts of biological tissue bring about changes in MR signal intensity, which in turn results in an imaging contrast. To validate the T_1- and T_2-weighted contrast ability, the relaxivity of the Fe_3O_4/CIS@SiO_2(Gd-DTPA)-RGD NPs in water at 3.0 T MR systems was examined (Fig. 6b c). As shown in Fig. 6b, the nanoparticle induced the signal enhancement in a concentration-dependent manner on the T_1-weighted images. The r_1 of the NPs was determined to be 1.56 mM^{-1} s^{-1} at 3.0 T MR systems, which was lower than that of Gd-DTPA (5.4 mM^{-1} s^{-1}).[45] It is reported previously that the r_1 values of Gd-based contrast agents were strengthened when bound to large molecules such as proteins and polymers due to the limited molecular motion of Gd^{3+} ions.[7] Hence, it was conceivable that the remarkably high r_1 value of the NPs resulted from the reduced mobility of Gd^{3+} ions tightly incorporated into nanometer-scale particles. Since the covalently immobilized DTPA shell on the NPs allows for strong coordination of Gd^{3+} ions onto the particles, the NPs are considered to be safer than aqueous $Gd(NO_3)_3$ solution. Likewise, all NPs also display a signal reduction in the T_2-weighted MRI images with the increase of Fe concentration. The r_2 relaxivity value for NPs was determined to be 23.22 mM^{-1} s^{-1} (Fig. 6c). After Gd^{3+} labeling, the r_2 relaxivity value of the NPs decreased obviously comparison with the reported,[14] which indicates that the paramagnetic Gd^{3+} chelates interfered with the T_2 relaxation processes of the neighboring magnetite NPs.[46,47] Even so, their T_2 contrast effect is sufficiently strong to generate negative contrast enhancement on the MR images in vivo.

3.3 Three mode fluorescent, T_1- and T_2- weight MR imaging of cancer cells in vitro. The cytotoxicity of Fe_3O_4/CIS@SiO_2(Gd-DTPA)-RGD NPs was evaluated using an MTT [3-(4,5-dimethylthiazol-2-yl)-2,5-diphenyltetrazolium bromide] assay with BXPC-3 cells, a human pancreatic cancer cell line (Fig. 7). The concentration-dependent effect of Fe_3O_4/CIS@SiO_2(Gd-DTPA)-RGD NPs on the cell viability at 3 and 24 h was determined. The results show that cytotoxicity of the NPs is low due to many factors, including the use of the elements with low toxicity. It is clear that the high cell viability can still be attained even at the NPs concentration of 2 mg mL^{-1}. This indicates that the Fe_3O_4/CIS@SiO_2(Gd-DTPA)-RGD NPs are biocompatible at Fe concentrations up to 2.4 mM.

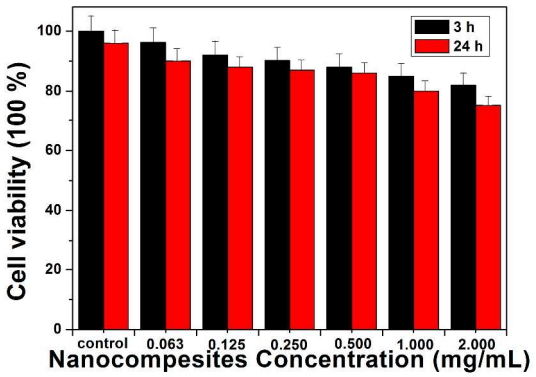

Fig. 7 Cytotoxicity evaluation of Fe_3O_4/CIS@SiO_2(Gd-DTPA)-RGD NPs in the BXPC-3 cells at different concentrations for 3 and 24 h at 37 °C.

To determine the potential of using these Fe_3O_4/CIS@SiO_2(Gd-DTPA)-RGD NPs with high relaxivity and photoluminescence as multimodal probes for in vitro fluorescence imaging in living cells, we incubated human pancreatic cancer cell lines BXPC-3 cells with the NPs for 3 h and then observed the cells with confocal microscopy. The targeting molecule, RGD, was covalently functionalized to the NPs via EDC/NHS binding. As shown in Fig. 8, it is clear that the BXPC-3 cells tagged with the NPs emitted clear red emission under 488 nm argon laser excitation, indicating that the NPs were readily internalized into human pancreatic cancer cells lines BXPC-3 cells.

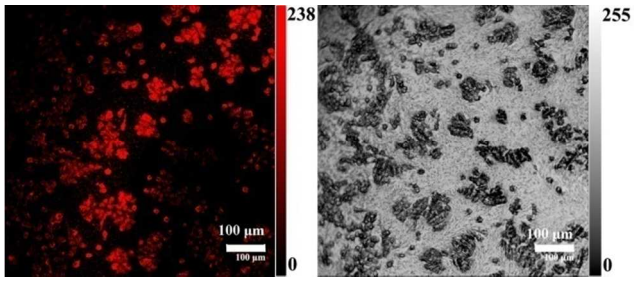

Fig. 8 Fluorescent image of BXPC-3 cells tagged with Fe_3O_4/CIS@SiO_2(Gd-DTPA)-RGD NPs with red emission under 488 nm argon laser excitation (right) and bright-field (right). Scale bar = 100 μm.

To further evaluate the feasibility of using MRI to detect cancer cells, the MR signal intensity of BXPC-3 cells treated with the Fe_3O_4/CIS@SiO_2(Gd-DTPA)-RGD NPs with different concentrations (0, 0.063, 0.125, 0.500, 1.000 and 2.000 mg mL^{-1}) were measured using a 3 T MRI system (Fig. 9). It is clear that BXPC-3 cells treated with the Fe_3O_4/CIS@SiO_2(Gd-DTPA)-RGD NPs show gradual both T_1- and T_2-weighted MR signal enhancement with increasing the concentration. Our results clearly show that Fe_3O_4/CIS@SiO_2(Gd-DTPA)-RGD NPs for T_1- and T_2 MRI have good spatial resolution, in agreement with literature data.[14] It is demonstrated that the same range of applied concentration can produce contrast for T_1- and T_2-weighted MR imaging dual-mode utility of the NPs would provide a novel candidate for cell imaging and biomedical.

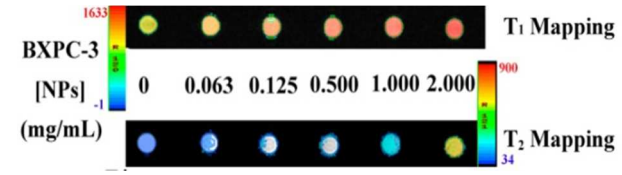

Fig. 9 T_1- and T_2-weighted MR images of Fe_3O_4/CIS@SiO_2(Gd-DTPA)-RGD NPs in BXPC-3 cells for 3 h incubation time (3 T MR system). The color bar changing from black to white indicates the gradual increase in MR signal intensity.

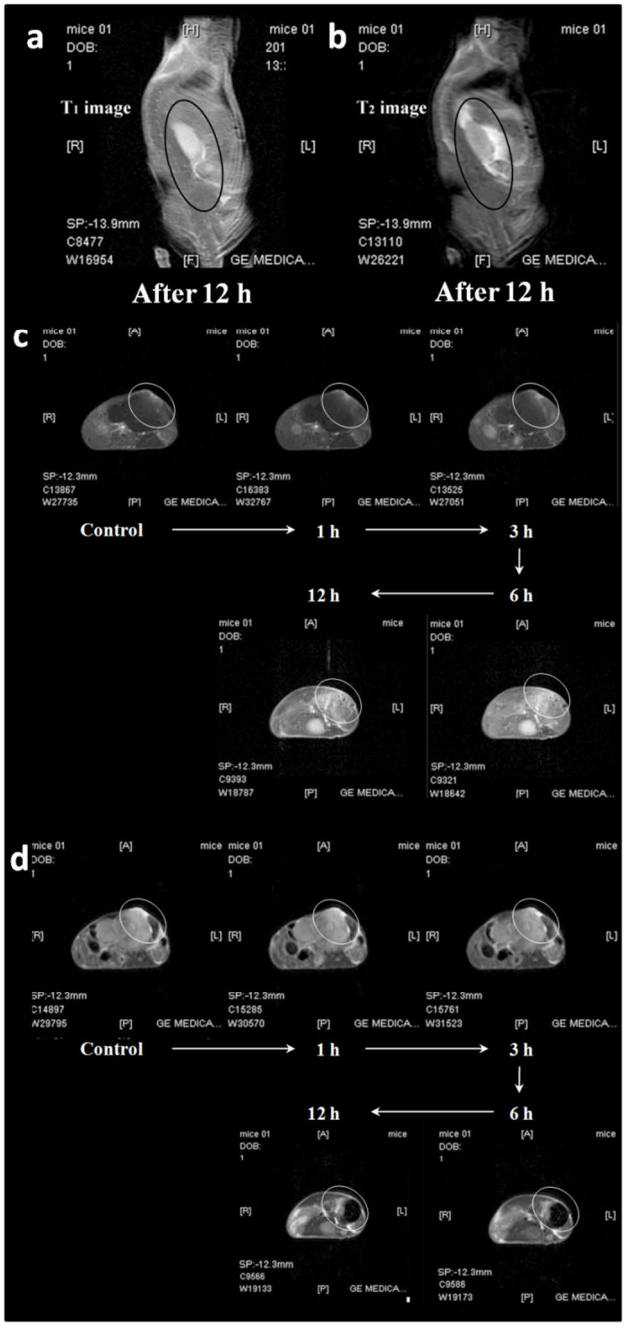

Fig. 10 (a) and (b) T_1- and T_2-weighted magnetic resonance images of entire abdomen injected with Fe_3O_4/CIS@SiO_2(Gd-DTPA)-RGD NPs after 12 h; (c) and (d) T_1- and T_2-weighted magnetic resonance images of pancreatic adenocarcinoma before injection, and 1 h, 3 h, 6 h and 12 h post injection.

3.4 Targeted MR imaging in vivo. The targeted dual mode MR imaging of cancer cells using Fe_3O_4/CIS@SiO_2(Gd-DTPA)-RGD NPs was further performed in vivo using an animal pancreatic adenocarcinoma model. Fe_3O_4/CIS@SiO_2(Gd-DTPA)-RGD NPs (200 mL, 16 mg per kg of mouse body weight) were injected into the mouse through its tail vein. The MRI study was performed on a clinical 3.0 T MR imaging system. Fig. 10 a and b show the T_1- and T_2-weighted images of entire abdomen obtained after injection 12 h. Fig. 10 c and d displayed the T_1- and T_2-weighted images of pancreatic adenocarcinoma obtained before injection, and 1 h, 3 h, 6 h and 12 h post injection, respectively. Compared with the image without particle injection, T_1- and T_2- weighted MR images of pancreatic adenocarcinoma at 1 h and 3 h post injection do not show obvious changes, which is presumably due to the fact that the Fe_3O_4/CIS@SiO_2(Gd-DTPA)-RGD NPs have not entered into the pancreatic adenocarcinoma site within such a short time. After 6 h post injection, the T_1 and T_2 MR images of the tumor show significant bright and darkened enhancement effect, respectively. And after 12 h, the signals are further enhanced. These results demonstrated that Fe_3O_4/CIS@SiO_2(Gd-DTPA)-RGD NPs with high r_1 and r_2 relaxivities exhibit both positive T_1 and negative T_2 contrast enhancement on the tumor MR images at the same time. Taken together with both in vitro and in vivo results related to the targeted T_1 and T_2 signal enhancing effects upon treatment of cancer cells with the Fe_3O_4/CIS@SiO_2(Gd-DTPA)-RGD NPs, the advantages of combination of the two agents (Gd(III) and Fe_3O_4) have been demonstrated fully.

4. Conclusions

In summary, we have demonstrate the facile fabrication of Gd-labeled surperparamagnetic Fe_3O_4 NPs and florescence CIS quantum dots conjugated with RGD peptides for tri-mode targeted T_1-, T_2-weighted MR and fluorescent imaging of cancer cells. These formed tri-mode multifunctional NPs are water-dispersible and display good biocompatibility with respect to *in vitro* cytotoxicity tests conducted by MTT assay on BXPC-3 cells. The great T_1 and T_2 relaxivities of the multifunctional NPs enable T_1- and T_2-weight MR imaging of cancer cells in vitro and in vivo. The MR imaging data clearly indicate that the multifunctional Fe_3O_4/CIS@SiO_2(Gd-DTPA)-RGD NPs can specifically target to cancer cells with $\alpha_v\beta_3$ integrin over-expression on the cell surface through receptor-mediated delivery pathway. The T_1-weight positive and T_2-weighted negative enhancement in the MR imaging significantly improve the diagnosis accuracy and fluorescent imaging of tumor tissue can assist in the clinical surgery. The developed Fe_3O_4/CIS@SiO_2(Gd-DTPA)-RGD NPs show a great potential for conjugating with other biomolecules (e.g., antibody, sugars, and peptides, etc.), thereby providing a unique platform for targeting and tri-mode imaging of other biological systems.

Acknowledgements

This work was supported by the National Natural Science Foundation of China (21136006, 21206043, 21236003, 21322607, 21406072 and 21471056), the Shanghai Shuguang

Scholars Program (13SG31), the Shanghai Rising-Star Program (13QA1401100), Program for Professor of Special Appointment (Eastern Scholar) at Shanghai Institutions of Higher Learning, Project funded by China Postdoctoral Science Foundation (2014M560307, 2014M561497), and the Fundamental Research Funds for the Central Universities.

Notes and references

[a] *Key Laboratory for Ultrafine Materials of Ministry of Education, School of Materials Science and Engineering, East China University of Science and Technology, Shanghai 200237, China. Fax: +86-21-64250624; E-mail: yhzhu@ecust.edu.cn; czli@ecust.edu.cn*

[b] *Shanghai Nanotechnology Promotion Center, Shanghai 200237, China*

[c] *Zhongshan Hospital of Fudan University, Shanghai Medical College of Fudan University, 138 Fenglin Road, Shanghai 200032, China*

[d] *Department of Surgery, Huashan Hospital, Fudan University, Shanghai 200040, China*

1. M. G. Keane, K. Bramis, S. P. Pereira, G. K. Fusai, *World J Gastroentero.* 2014, **20**, 2267.
2. G. Garcea, A. R. Dennison, C. J. Pattenden, C. P. Neal, C. D. Sutton, D. P. Berry, *JOP J Pancreas.* 2008, **9**, 99.
3. S. Egawa, H. Toma, H. Ohigashi, T. Okusaka, A. Nakao, T. Hatori, H. Maguchi, A. Yanagisawa, M. Tanaka, *Pancreas* 2012,**41**, 985.
4. W. Schima, A. Ba-Ssalamah, C. Kölblinger, C. Kulinna-Cosentini, A. Puespoek, P. Götzinger, *Eur. Radiol.* 2007, **17**, 638.
5. B. Shah, P. T. Yin, S. Ghoshal, K. B. Lee, *Angew. Chem., Int. Ed.* 2013, **52**, 6190.
6. R. D. Corato, F. Gazeau, C. L. Visage, D. Fayol, P. Levitz, F. Lux, D. Letourneur, N. Luciani, O. Tillement, C. Wilhelm, *ACS Nano*, 2013, **7**, 7500.
7. M. F. Kircher, A. Zeral, J. V. Jokerst, C. L. Zavaleta, P. L. Kempen, E. Mittra, K. Pitter, R. Huang, C. Campos, F. Habte, R. Sinclair, C. W. Brennan, I. K. Mellinghoff, E. C. Holland, S. S. Gambhir, *Nat. Med.* 2012, **18**, 829.
8. S. Aime, M. Fasano, E. Terreno, *ChemSoc Rev.* 1998, **27**, 19.
9. P. Caravan, *Chem. Soc. Rev.* 2006, **35**, 512-523.
10. K. N. Raymond, V. C. Pierre, *Bioconjug Chem.* 2004, **16**, 3.
11. D. Peer, J. M. Karp, S. Hong, O. C. Farokhzad, R. Margalit, R. Langer, *NatNanotechnol.* 2007, **2**, 751.
12. H. Lee, E. Lee, D. K. Kim, N. K. Jang, Y. Y. Jeong, S. Jon, *J. Am. Chem. Soc.* 2006, **128**, 7383.
13. G. H. Im, S. M. Kim, D. G. Lee, W. J. Lee, J. H. Lee, I. S. Lee, *Biomaterials* 2013, **34**, 2069.
14. H. Yang, Y. Zhuang, Y. Sun, A. Dai, X. Shi, D. Wu, F. Li, H. Hu, S. Yang, *Biomaterials* 2011, **32**, 4584.
15. J. Liu, W. Zhang, H. Zhang, Z. Yang, T. Li, B. Wang, X. Huo, R. Wang, H. Chen, *Chem. Commun.* 2013, **49**, 4938.
16. N. Lee, H. Kim, S. H. Choi, M. Park, D. Kim, H. C. Kim, Y. Choi, S. M. Lin, B. H. Kim, H. S. Jung, H. Kim, K. S. Park, W. K. Moon, T. Hyeon, *Proc. Natl. Acad. Sci. U. S. A.* 2011, **108**, 2662.
17. H. Yang, Y. Zhuang, H. Hu, X. Du, C. Zhang, X. Shi, H. Wu, S. Yang, *Adv. Funct. Mater.* 2010, **20**, 1733.
18. G. Hong, J. T. Robinson, Y. J. Zhang, S. Diao, A. L. Antaris, Q. B. Wang, H. Dai, *Angew. Chem., Int. Ed.* 2012, **51**, 9818.
19. I. Hocaoglu, M. N. Cizmeciyan, R. Erdem, C. Ozen, A. Kurt, A. Sennaroglu, H. Y. Acar, *J. Mater. Chem.* 2012, **22**, 14674.
20. P. Jiang, C. N. Zhu, Z. L. Zhang, Z. Q. Tian, D. W. Pang, *Biomaterials* 2012, **33**, 5130.
21. M. Oostendorp, K. Douma, M. T. Hackeng, J. M. Post, M. A. van Zandvoort, W. H. Backes,*Magn. Reson. Med.* 2010, **64**, 291.
22. R. Bakalova, Z. Zhelev, I. Aoki, K. Masamoto, M. Mileva, T. Obata, M. Higuchi, V. Gadjeva, I. Kanno, *Bioconjugate Chem.* 2008, **19**, 1135.
23. P. Diagaradjane, A. Deorukhkar, J. G. Gelovani, D. M. Maru, S. Krishnan, *ACS Nano* 2010, **4**, 4131.
24. J. Park, S. Bhuniya, H. Lee, Y. W. Noh, T. Y. Lim, H. J. Jung, S. K. Hong, S. J. Kim, *Chem. Commun.* 2012, **48**, 3218.
25. L. Liu, W. C. Law, K. T. Yong, I. Roy, H. Ding, F. Erogbogbo, X. Zhang, P. N. Prasad, *Analyst* 2011, **136**, 1881.
26. A. M. Derfus, W. C. W. Chan, S. N. Bhatia, *Nano Lett.* 2004, **4**, 11.
27. A. L. Morel, S. I. Nikitenko, K. Gionnet, A. Wattiaux, J. Lai-Kee-Him, C. Labrugere, B. Chevalier, G. Deleris, C. Petibois, A. Brisson, M. Simonoff, *ACS Nano*2008, **2**, 847.
28. I. Ruach-Nir, T. A. Bendikov, I. Doron-Mor, Z. Barkay, A. Vaskevich, I. Rubinstein, *J. Am. Chem. Soc.* 2007, **129**, 84.
29. A. J. Beer, M. Schwaiger, *Cancer Metastasis Rev.* 2008, **27**, 631.
30. K. Chen, J. Xie, H. Xu, D. Behera, M. H. Michalski, S. Biswal, A. Wang, X. Chen, *Biomaterials* 2009,**30**, 6912.
31. M. A. Dechantsreiter, E. Planker, B. Mathä, E. Lohof, G. Hölzemann, A. Jonczyk, S. L. Goodman, H. Kessler, *J Med Chem.* 1999, **42**, 3033.
32. T. J. Wadas, H. Deng, J. E. Sprague, A. Zheleznyak, K. N. Weilbaecher, C. J. Anderson, *J Nucl Med.* 2009, **50**, 1873.
33. J. Park, K. An, Y. Hwang, J. Park, H. Noh, J. Kim, J. Park, N. Hwang, T. Hyeon, *Nat. Mater.* 2004,**3**, 891.
34. B. Lin, X. Yao, Y. Zhu, J. Shen, X. Yang, C. Li, *RSC Adv.* 2014, **4**, 20641.
35. B. Lin, X. Yao, Y. Zhu, J. Shen, X. Yang, H. Jiang, X. Zhang, *New J. Chem.* 2013, **37**, 3076.
36. J. Kim, H. S. Kim, N. Lee, T. Kim, H. Kim, T. Yu, I. C. Song, W. K. Moon, T. Hyeon, *Angew. Chem., Int. Ed.* 2008, **47**, 8438.
37. J. Kim, J. E. Lee, J. Lee, J. H. Yu, B. C. Kim, K. An, Y. Hwang, C. H. Shin, J. G. Park, J. Kim, T. Hyeon, *J. Am. Chem. Soc.* 2006, **128**, 688.
38. L. Li, T. J. Daou, I. Texier, T. T. K. Chi, N. Q. Liem, P. Reiss, *Chem. Mater.* 2009, **21**, 2422.
39. H. Zhong, S. S. Lo, T. Mirkovic, Y. Li, Y. Ding, Y. Li, G. D. Scholes, *ACS Nano* 2010, **4**, 5253.
40. P. J. Debouttière, S. Roux, F. Vocanson, C. Billotey, O. Beuf, A. Favre-Réguillon, Y. Lin, S. Pellet-Rostaing, R. Lamartine, P. Perriat, O. Tillement, *AdvFunct Mater.* 2006, **16**, 2330.
41. M. Uehara, K. Watanabe, Y. Tajiri, H. Nakamura, H. Maeda, *J. Chem. Phys.* 2008, **129**,134709.
42. Y. Zhu, J. Shen, K. Zhou, C. Chen, X. Yang, C. Li, *J. Phys. Chem. C* 2011, **115**, 1614.
43. Q. L. Fan, K. G. Neoh, E. T. Kang, B. Shuter, S. C. Wang, *Biomaterials* 2007, **28**, 5426.
44. S. A. Empeedocles, M. G. Bawendi, *Science* 1997, *278*, 2114.
45. K. H. Bae, Y. B. Kim, Y. Lee, J. Hwang, H. Park, T. G. Park, *Bioconjug. Chem.* 2010, **21**, 505.
46. A. Villringer, B. R. Rosen, J. W. Belliveau, J. L. Ackerman, R. B. Lauffer, R. B. Buxton, Y. S. Chao, V. J. Wedeen, T. J. Brady,*Magn. Reson. Med.* 1988, **6**, 164.
47. P. Loubeyre, T. De Jaegere, H. Bosmans, Y. Miao, Y. Ni, W. Landuyt, G. Marchal, *J. Magn. Reson. Imag.* 1999, **9**, 447.